

Mechanical topological semimetals with massless quasiparticles and a finite Berry curvature

Guanglei Wang,¹ Hongya Xu,¹ and Ying-Cheng Lai^{1,2,*}

¹School of Electrical, Computer, and Energy Engineering, Arizona State University, Tempe, Arizona 85287, USA

²Department of Physics, Arizona State University, Tempe, Arizona 85287, USA

(Received 1 May 2017; published 30 June 2017)

A topological quantum phase requires a finite momentum-space Berry curvature which, conventionally, can arise through breaking the inversion or the time-reversal symmetry so as to generate nontrivial, topologically invariant quantities associated with the underlying energy band structure (e.g., a finite Chern number). For conventional graphene or graphenelike two-dimensional (2D) systems with gapless Dirac cones, the symmetry breaking will make the system insulating due to lifting of the degeneracy. To design materials that simultaneously possess the two seemingly contradicting properties (i.e., a semimetal phase with gapless bulk Dirac-like cones and a finite Berry curvature) is of interest. We propose a 2D mechanical dice lattice system that exhibits precisely such properties. As a result, an intrinsic valley Hall effect can arise without compromising the carrier mobility as the quasiparticles remain massless. We also find that, with confinement along the zigzag edges, two distinct types of gapless edge states with opposite edge polarizations can arise, one with a finite but the other with zero group velocity.

DOI: 10.1103/PhysRevB.95.235159

I. INTRODUCTION

Topology has become a fundamental and powerful principle to understand and characterize the exotic phases of condensed matter systems, leading to the discovery of topological materials such as topological insulators, topological superconductors, and topological metals [1–6]. The invariant quantity used to characterize the novel topological states is the Chern number calculated by integrating the Berry curvature within the whole Brillouin zone [7]. The Berry curvature defined in the momentum space as the Berry phase density plays a similar role to that of a magnetic field in the position space. Associated with topological transport, a Bloch electron will experience an anomalous velocity induced by the finite Berry curvature according to the semiclassical picture [7–10]. This is the fundamentally intrinsic mechanism for the anomalous Hall effect [11] and valley Hall effect [10].

In two-dimensional (2D) systems, the valley Hall effect was first theorized [10] for graphene [12,13]. Despite the weak spin-orbit interaction intrinsic to graphene, it possesses two nonequivalent valleys at the corners of the Brillouin zone, which are separated by a large momentum. As a result, there is strong suppression of intervalley scattering, making the valley index an additional quantum number to describe the electronic state. Conventionally, a finite Berry curvature can arise in systems with a broken inversion symmetry, and a finite Chern number requires further breaking of the time-reversal symmetry [7]. For graphene, according to the Haldane model [14], the interactions required for breaking the inversion or the time-reversal symmetry will generically remove the degeneracy of the pair of Dirac cones at their interaction point, opening an energy gap [10,15,16]. In addition to graphene, 2D Chern semimetals have been proposed for the Lieb lattice, but there is still a direct band-gap opening [17]. Nonetheless,

topological phases in gapless bulk systems can occur but in three dimensions, such as the Weyl [18–20] and Dirac [21,22] semimetals.

In this paper, we ask the following question: is it possible to have a 2D system with a finite Berry curvature but without any direct band-gap opening? If yes, then novel topological quantum phases can occur with massless quasiparticles. To address this question and to obtain a physical understanding, we exploit the mechanical analog of the electronic systems. Indeed, recently the counterparts of a number of electronic phenomena such as Dirac cones, the quantum (anomalous) Hall state, and topologically protected edge states, have been realized in classical mechanical systems [23–35], leading to the emergence of a new field: topological phononics [25,28,29,36]. In such a system (and also in photonic systems), the nontrivial topological phase is fundamentally a wave phenomenon [24], opening the door to probing into topology-based physics through the classical approach. Compared with electronic systems, classical mechanical systems as governed by the Newton's laws have the advantage of superior controllability and feasible experimental implementability.

The main accomplishments of this paper are the following. We utilize the classical spring-mass model to construct a mechanical dice lattice system, a combination of two honeycomb lattices with a relative displacement. Such a lattice for electronic systems has a threefold band degenerate structure with an emerging flatband and features *massless* spinor quasiparticles [37]. Through a detailed exploration of the parameter space for the proposed mechanical system, we find regions of nonzero measure with three-band or two-band degeneracies, about which the energy momentum dispersion has a conical structure—the characteristic signature of massless quasiparticles. A key result is that there is naturally an inversion symmetry breaking with the degeneracy maintained through modifying the spring constant of one subset of the dice lattice. This leads to a finite Berry curvature and, consequently, to a *mechanical topological*

*Ying-Cheng.Lai@asu.edu

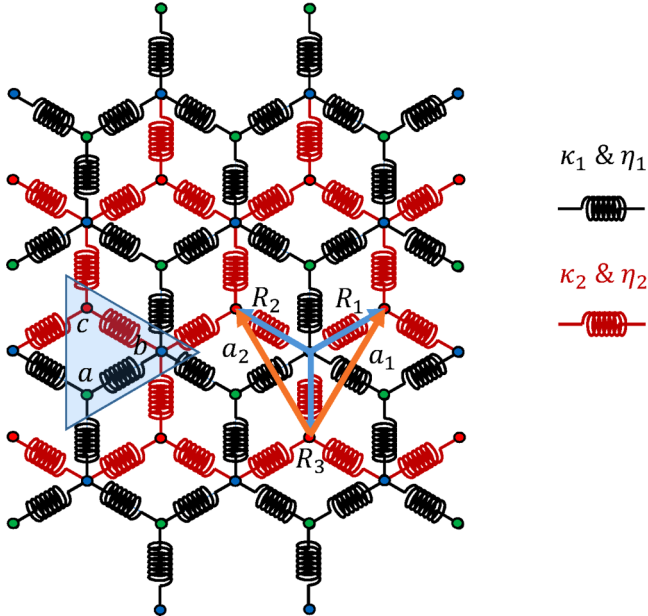


FIG. 1. Schematic illustration of our mechanical dice lattice. The two subsets of honeycomb lattices are colored by black and red, with respective spring parameters κ_1, η_1 and κ_2, η_2 . All the mass points are identical but can be physically nonequivalent. There are three mass points in one unit cell, which are colored by red, blue, and green. With unequal spring constants for the two subsets, there is naturally an inversion symmetry breaking.

semimetal phase. We also study the ribbon geometry and find gapless edge states with opposite conducting properties, e.g., there can be a conducting channel along one edge but a nonconducting channel along the other edge. These results not only are relevant to the field of topological phononics, but also provide insights into the possible realization of 2D electronic materials exhibiting nontrivial topological quantum phases with massless quasiparticles.

II. MECHANICAL LATTICE MODEL

We consider a mechanical dice lattice, motivated by the recently studied mechanical honeycomb lattice [23,24], in which atoms are modeled as identical mass points and any pair of neighboring atoms is coupled through a spring of constant κ_1 (or κ_2) and a natural length l_0 . As shown in Fig. 1, the lattice is a superposition of two honeycomb lattices with a relative displacement. Differing from the existing works [23,24], in our lattice each unit cell contains three atoms. At the equilibrium, the spring length R_0 is not necessarily equal to the natural length l_0 . It is thus convenient to use $\eta = l_0/R_0$ as a parameter to characterize the spring. Note that a threefold rotational symmetry always holds in the system regardless of the parameter values, while the spatial inversion symmetry can be broken for $\kappa_1 \neq \kappa_2$ or $\eta_1 \neq \eta_2$. The static equilibrium of the bulk mass points is guaranteed by the symmetry of the dice lattice while the states of the boundary mass points are determined by the boundary conditions. We restrict the motion to 2D and focus on small displacements about the equilibrium points. For the mass points in the unit cell, the dynamical variables are their deviations from the static equilibrium

positions: $\mathbf{x}_r = (x_{r,a}, y_{r,a}, x_{r,b}, y_{r,b}, x_{r,c}, y_{r,c})^T$, where \mathbf{r} denotes the unit-cell lattice coordinate and a, b, c are the three mass points in one unit cell. In general, the two honeycomb lattices have different parameters, so the three mass points in the unit cell are not equivalent to each other.

The motions of atoms are described by the classical Hamilton's equations. For example, for one degree of freedom we have $m\ddot{x} + \partial H/\partial x = 0$. For simplicity, we assume unit mass for all the atoms in the lattice. Only the nearest-neighboring terms in the Hamiltonian H contribute to the motions. We assume that the springs are in the linear regime so that the elastic potential of an individual spring can be written as $U_s = (\kappa/2)(l - l_0)^2$, with l being the instantaneous length of the spring. For motion about the equilibrium position, we apply Taylor expansion up to the second order. Changing the dynamical variables from the real \mathbf{r} space into the momentum \mathbf{k} space [23],

$$z_{r,v} = \frac{1}{N} \sum_k e^{i\omega t + i\mathbf{k} \cdot \mathbf{r}} \phi_z^v(\mathbf{k}), \quad (1)$$

where $z \in \{x, y\}$ and $v \in \{a, b, c\}$, we obtain the eigenfunctions of the dynamic matrix, which yields the frequency spectrum as

$$\omega^2 \phi(\mathbf{k}) = \Gamma(\mathbf{k}) \phi(\mathbf{k}), \quad (2)$$

where $\phi(\mathbf{k}) = [\phi_x^a(\mathbf{k}), \phi_y^a(\mathbf{k}), \phi_x^b(\mathbf{k}), \phi_y^b(\mathbf{k}), \phi_x^c(\mathbf{k}), \phi_y^c(\mathbf{k})]^T$,

$$\Gamma(\mathbf{k}) = \begin{bmatrix} \Lambda_1 & \Gamma_{ab}(\mathbf{k}) & 0 \\ \Gamma_{ab}^\dagger(\mathbf{k}) & \Lambda_1 + \Lambda_2 & \Gamma_{bc}(\mathbf{k}) \\ 0 & \Gamma_{bc}^\dagger(\mathbf{k}) & \Lambda_2 \end{bmatrix}, \quad (3)$$

and

$$\Lambda_i = 3\kappa_i \left(1 - \frac{\eta_i}{2}\right) \hat{l}_2,$$

$$\Gamma_{ab}(\mathbf{k}) = -\kappa_1 (\gamma_{R_1}^{xy} e^{ik \cdot a_1} + \gamma_{R_2}^{xy} e^{ik \cdot a_2} + \gamma_{R_3}^{xy}),$$

$$\Gamma_{bc}(\mathbf{k}) = -\kappa_2 (\gamma_{R_1}^{xy} + \gamma_{R_2}^{xy} e^{-ik \cdot (a_1 - a_2)} + \gamma_{R_3}^{xy} e^{-ik \cdot a_1}),$$

with $\gamma_{R_i}^{xy} \equiv [1 - \eta, \eta R_{i,x} R_{i,y}; \eta R_{i,y} R_{i,x}, 1 - \eta]$. In these expressions, $R_{i,x}$ and $R_{i,y}$ ($i = 1, 2, 3$) are the x, y components of the R vectors shown in Fig. 1, $a_1 = (1/2, \sqrt{3}/2)a$, $a_2 = (-1/2, \sqrt{3}/2)a$, and a is the length of the primitive basis vectors. Equation (2) represents a six-dimensional eigenvalue problem. The frequencies ω are given by the square root of the eigenvalues of Eq. (2). Negative eigenvalues lead to a pair of purely imaginary values of ω , which depend upon the system parameters and correspond to unstable eigenstates that can be excluded from our calculation of the energy bands.

As shown in Fig. 1, our mechanical dice lattice constitutes two honeycomb lattices with parameters (κ_1, η_1) (black) and (κ_2, η_2) (red). The parameter space for the lattice system is thus four dimensional: $\{\kappa_1, \eta_1, \kappa_2, \eta_2\}$. From Eq. (3), we see that the parameters (κ_1, κ_2) only appear as the scaling factors in both diagonal elements, representing the weight of each sublattice and off-diagonal elements characterizing the mutual coupling strength between sublattices. We thus set $\kappa_1 = 1$, which is equivalent to scaling κ_2 as κ_2/κ_1 . For more complicated interactions such as the Coriolis force that breaks the time-reversal symmetry, it is not possible to relate

the frequency ω directly to the eigenvalues. This difficulty can be overcome by introducing a Schrödinger-like equation for phonons [25] so that the concept of wave function and topology-related quantities can be naturally introduced into the mechanical lattice system.

III. PHASE DIAGRAMS AND HIGHLY DEGENERATE STATES

Highly degenerate states and the approximate dispersion relations associated with the states are of physical interest. Since the rescaled parameter space is three dimensional, $\{\eta_1, \kappa_2, \eta_2\}$, we fix the value of η_1 to calculate the phase diagram in the $\kappa_2 - \eta_2$ parameter plane. Because of the difficulty in carrying out numerical characterization of the band structure in an automated fashion, we exploit analytic solutions to detect the parameter regions in which degeneracies occur (detailed below). Representative results are shown in Fig. 2.

A characteristic feature of an electronic dice lattice is that it has a three-band degenerate point at which a flatband intersects with the degenerate point of the conventional Dirac cones. The main goal of our work is to investigate whether such a three-band degenerate point exists in the mechanical dice lattice system. To achieve this, we first obtain analytic solutions of the eigenvalue spectrum from a reduced 4×4 dynamic matrix (see Appendix) for each parameter pair from a fine grid covering the parameter plane. We then determine the parameter values

that lead to a three-band degeneracy. Figure 2(a) shows, for $\eta_1 = 0$, the analytically determined curves along which there is an exact three-band degeneracy (the solid red curves). Away from a point on the curves, there is an approximate three-band degeneracy, but the third band is lifted slightly, opening a gap of size proportional to the parameter distance from the red curve. The shaded/fading regions containing the curves thus represent parameter regions in which the gap between the third band and the two-band degeneracy point is insignificant. Physically these regions exhibit an approximate three-band degeneracy that is potentially accessible to experimental observations. The blank areas in Fig. 2(a) correspond to the parameter regions of an exact two-band degeneracy. Figures 2(b)–2(e) show the typical band structures from the four red curves, with the parameters specified by the cyan points. Note that since we focus on physically realizable stable solutions, we ignore the purely imaginary band so that the total number of bands is less than six. The band structure with a small value of κ_2 is similar to that of mechanical graphene but has a triply degenerate point, as shown in Fig. 2(b). Notably, Fig. 2(c) shows a different gapless profile of the degeneracy of the same fold, which is similar to that in an electrical dice lattice near the degenerate point. In Fig. 2(c), the green and yellow bands form a pair of Dirac cones at the $K(K')$ point which intersect with a third flat purple band. The band structure in Fig. 2(d) is analogous to that characterizing massive Dirac quasiparticles

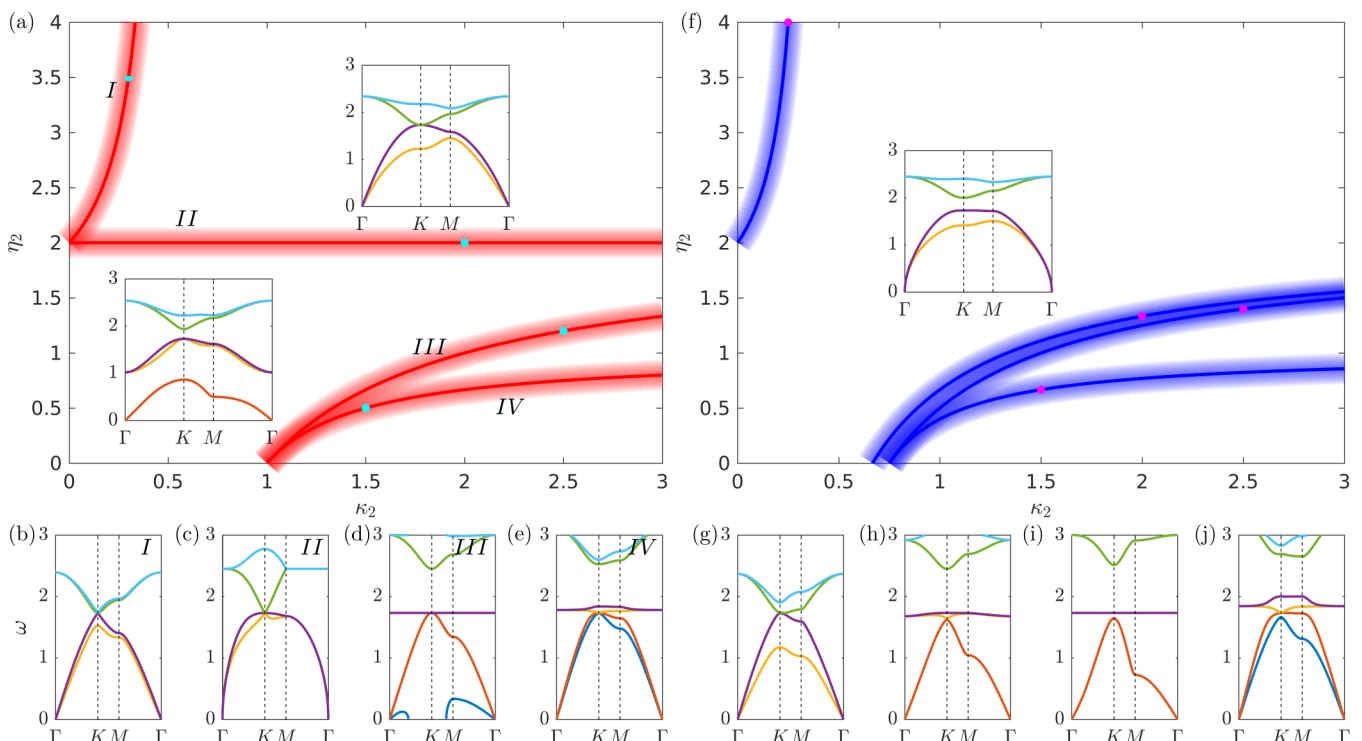


FIG. 2. Phase diagrams of proposed mechanical dice lattice system. (a) For $\eta_1 = 0$, three-band degenerate phases (shaded/fading areas containing the red curves) and two-band degenerate phases (the blank areas). Insets are examples of the two-band degenerate phases. (b–e) Typical band structures in the three-band degenerate phase, with parameters marked by the cyan points in (a). (f) Phase diagram for $\eta_1 = 0.5$, where the two-band degenerate phases are shown as shaded/fading areas containing the blue curves and the blank areas correspond to parameter regions with no degeneracy (inset: an example of nondegenerate band structure). (g–j) Typical structures of two-band degeneracy for parameter values marked by the magenta points in (f).

based on the two dispersive bands about the K point, with the exception that there are two additional coincident flatbands intersecting with the orange dispersive band. Figure 2(e) shows the six bands in the entire momentum space, where another triply degenerate point emerges with a different dispersion profile. From Figs. 2(b)–2(e), we see that the number of bands above the three degenerate points changes gradually, e.g., from zero in Fig. 2(b) to three in Fig. 2(e). The emerging triply degenerate points and the conical-like dispersion about them are evidence of the classical mechanical analog of triple point metals with massless quasiparticles beyond the canonical Dirac/Weyl paradigm [38,39].

In different parameter regimes, our mechanical dice lattice system can exhibit features of the two-band structure as in mechanical graphene. Figure 2(f) shows, for $\eta_1 = 0.5$, the phase diagram with κ_2 and η_2 varying in the ranges from 0 to 3 and from 0 to 4, respectively. The solid blue curves represent results from the analytic solutions along which an exact two-band degeneracy occurs, and the shaded/fading regions containing the curves indicate regions in which an approximate two-band degeneracy can arise. Figures 2(g)–2(j) present typical band structures corresponding to the four two-band degenerate phases with parameters marked by the magenta dots in Fig. 2(f). From Fig. 2(i), we find no isolated degenerate points, as the middle two bands coincide with each other along different paths in the \mathbf{k} space. A comparison between Figs. 2(g) and 2(j) indicates that the former exhibits pronounced features typical of a mechanical graphene system [23–27] while the latter exhibits six-band features. This can be understood in that, as κ_2 is decreased, the connection between the two subhoneycomb lattices is weakened. In the extreme case of $\kappa_2 = 0$, the band structure is reduced to that of mechanical graphene, regardless of the value of η_2 . On the opposite side, the emergence of the flatband is a strong indication that the system is no longer mechanical graphene. The blank areas in Fig. 2(f) specify parameter regions in which no degeneracies arise. A typical nondegenerate band structure is shown in the inset.

Note that from the spectrum equation for a given Bloch wave vector \mathbf{k} [Eq. (2)], the normal mode frequencies ω are the square roots of the eigenvalues of the matrix $\Gamma(\mathbf{k})$, which is originated from the second-order time derivative in the Newton's equations of motion. Depending on the system parameters κ and η , ω^2 can be negative, giving rise to unstable collective oscillation modes/exitations. In the domain of the real part of the frequency versus the momentum characterizing the band-structure profiles as in Fig. 2, the negative eigenvalues are physically irrelevant. In fact, there are regions of finite area in the parameter space where all six eigenfrequencies are real. For example, the lowest shaded regions in Figs. 2(a) and 2(b) have all six real frequencies, with two representative cases shown in Figs. 2(e) and 2(j), respectively.

To gain theoretical insights into the phase diagrams, we carry out an analysis to distinguish the band structures by expanding the dynamic matrix $\Gamma(\mathbf{k})$ about the $K = [2\pi/(3a), 2\pi/(\sqrt{3}a)]$ and $K' = [-2\pi/(3a), 2\pi/(\sqrt{3}a)]$ points and keeping the lower-order terms. As $\Gamma(\mathbf{k})$ is a 6×6 matrix, it is difficult to obtain explicit analytical expressions for the eigenvalues. However, since the maximum degeneracy occurs at the $K(K')$ points, we can focus on the energy levels at these

points. The frequency squared at the K point is

$$\omega^2 = \begin{cases} 3 - \frac{3}{2}\eta_1, \\ 3\kappa_2 - \frac{3}{2}\eta_2\kappa_2, \\ \frac{3}{4}[4 - 2\eta_1 - (-2 + \eta_2)\kappa_2 \pm \sqrt{4\eta_1^2 + (-2 + \eta_2)^2\kappa_2^2}], \\ \frac{3}{4}[2 - \eta_1 - 2(-2 + \eta_2)\kappa_2 \pm \sqrt{(-2 + \eta_1)^2 + 4\eta_2^2\kappa_2^2}]. \end{cases}$$

Setting $\eta_1 = 0$, we obtain two bands at $\omega^2 = 3$, regardless of the values of κ_2 and η_2 . To achieve a three-band degeneracy, we adjust the values of κ_2 and η_2 to make an additional band cross the $\omega^2 = 3$ point. We then get

$$\eta_2 = \begin{cases} 2 \rightarrow \text{Band II} \\ 2 - \frac{2}{\kappa_2} \rightarrow \text{Band III} \\ 1 + \frac{1}{1-2\kappa_2} \rightarrow \text{Band I/IV} \end{cases}$$

which defines the curves in the parameter plane along which three-band degeneracies occur. In Fig. 2(a), the solid red curves I and IV share the same $\eta_2(\kappa_2)$ relation, as they correspond to

$$\omega^2 = \frac{3}{4}[2 - \eta_1 - 2(-2 + \eta_2)\kappa_2 \pm \sqrt{(-2 + \eta_1)^2 + 4\eta_2^2\kappa_2^2}].$$

The physical picture here is that, in the limit $\eta_1 = 0$ (see Appendix for details), one of the three nonequivalent mass points, e.g., the green mass point in Fig. 1, can be decoupled from the other two about the $K(K')$ point, up to the first order. The two decoupled bands are degenerate at the $K(K')$ point, and a three-band degeneracy can be achieved insofar as the remaining four bands cross $\omega^2 = 3$. A similar analysis applies to the results in Fig. 2(f).

A direct consequence of the parameter differences in the two subhoneycomb lattices is the breaking of the inversion symmetry. In our proposed mechanical system, the broken inversion symmetry does not necessarily lift the conical-like degeneracy that is the characteristic signature of the massless nature of the quasiparticles in the semimetal phase. It is useful to investigate the effects of the inversion symmetry breaking in terms of the topology-related quantities, as will be described next.

IV. ANOMALOUS VALLEY HALL EFFECT IN SEMIMETAL PHASE

To probe into the topological properties of lattice systems with a three-band degeneracy, we first calculate the Berry curvature underlying the occupied Bloch states. In electronic systems, in the presence of an in-plane electric field, an electron will acquire an anomalous velocity proportional to the Berry curvature in the transverse direction [6–11], leading to anomalous quantum Hall and anomalous valley Hall effects. Based on symmetry considerations, in the momentum space, we have that the Berry curvature,

$$\Omega_n(\mathbf{k}) = \nabla_{\mathbf{k}} \times \langle \phi_n(\mathbf{k}) | i \nabla_{\mathbf{k}} | \phi_n(\mathbf{k}) \rangle,$$

is odd in the presence of a time-reversal symmetry and even in the presence of an inversion symmetry, where the subscript n denotes the band index and $\phi(\mathbf{k})$ is the Bloch wave defined in Eq. (2). When both time-reversal and inversion

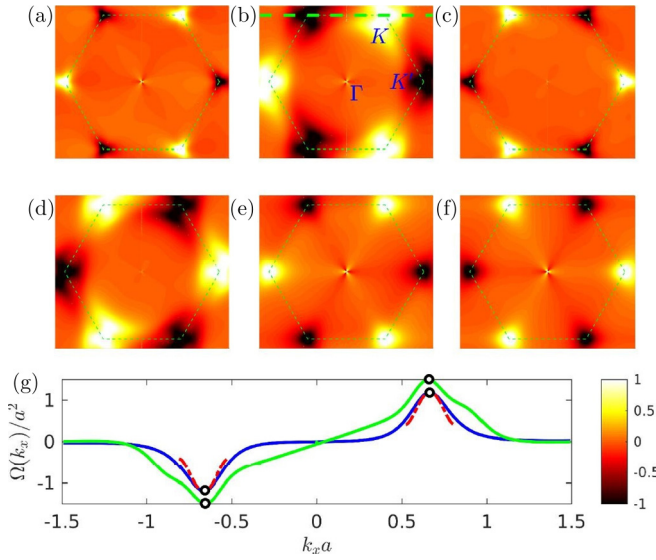


FIG. 3. Numerical and analytic results of Berry curvature. (a–f) Berry curvatures for the six bands of a threefold degenerate configuration, respectively. (g) Comparison between the numerical (blue solid curve) and analytical (red dashed curve segments) results from the reduced 4×4 dynamic matrix. The green curve is numerical result shown in (b) calculated from the original 6×6 dynamic matrix. The small black circles in (g) indicate the small neighborhoods of the K (K') points in which the numerical curvature values are not reliable. The parameters used are $\eta_1 = 0$, $\kappa_2 = 1.5$, and $\eta_2 = 0.5$, which are the same as in Fig. 2(e).

symmetries are present, the Berry curvature is zero over the whole Brillouin zone, except at the zero-measure degeneracy points (singularities) for semimetals.

Our mechanical dice lattice system preserves the time-reversal symmetry, while the inversion symmetry can be broken. We thus expect the Berry curvature in the Brillouin zone to be nonzero and an odd function of the wave vector. The Chern number, which is the integral of the Berry curvature within the entire Brillouin zone, is zero due to the time-reversal symmetry. However, the local finite Berry curvature with opposite signs for the two nonequivalent valleys can lead to an anomalous valley Hall effect in the semimetal phase, which cannot arise in conventional, Haldane-model-based electronic systems.

Figures 3(a)–3(f) show the Berry curvature for the six bands associated with the threefold degenerate configuration of Fig. 2(e). We see that across the Brillouin zone the Berry curvature is finite and assumes relatively large values about the K (K') points. It is also apparent that the Berry curvature possesses an odd inversion symmetry with respect to the Γ point, due to the time-reversal symmetry. Analytic results of the Berry curvature about the K (K') points are shown as the red dashed line in Fig. 3(g), with the blue solid line representing the numerical result for comparison. The results represented by the red and blue colors are obtained through a reduced, 4×4 dynamic matrix (see Appendix), while the green curve is the numerical result calculated directly from the 6×6 matrix. Since the Berry curvature depends on the normalized Bloch wave, a dimension reduction can cause small modifications to the value of the curvature, which is responsible for the

differences between the blue and green curves about the K (K') points. However, these two curves have similar features. For the reduced dynamic matrix, due to the small deviations about the K (K') points, we expect disagreement away from these points. There is a good agreement between analytic and numerical results, especially in terms of the sign, the value, and the trend of the curvature. The valley-contrasting Berry curvature will induce an anomalous velocity perpendicular to the external driving field, leading to an anomalous valley Hall effect in the semimetal phase. In practice, the driving field can be generated via an in-plane gradient strain [40]. Alternatively, one can follow the scheme of applying a Gaussian pulse source, as proposed in a more recent work [41], to observe and realize nontrivial valley-contrasting physics in the proposed mechanical lattice system. While the results in Figs. 3(a)–3(g) are for the limiting case $\eta_1 = 0$, similar phenomena have been observed for $\eta_1 = 0.5$, where there is an inversion symmetry breaking.

For the system to exhibit a finite Chern number, one can introduce a Coriolis force. In particular, when the classical system rotates uniformly with angular frequency Ω_a , the point with mass m and velocity \mathbf{v} will experience a force proportional to $m\mathbf{v} \times \Omega_a$. This is equivalent to the Lorentz force for charged particles under a magnetic field.

We note that, in general, at the degenerate (singular) points, the Berry curvature is ill defined. However, what really matters for the emergence of the topological states is finite Berry curvature *away* from the gapless points in the semimetal phase (from the corresponding band structure). This is precisely the feature that distinguishes our lattice from the conventional systems, with a vanishing Berry curvature away from the gapless Dirac points, e.g., graphene, making our system a mechanical analog of topological semimetal. While in a conventional system the Berry curvature values at the Dirac points are divergent, they are physically irrelevant. For the triply degenerate band profile arising from our lattice system, what is shown in Fig. 3 is the curvature values away from the K and K' points. Arbitrarily close to these points, an accurate calculation of the Berry curvature is not feasible. Nonetheless, as discussed, the divergent curvature values at the Dirac points are not essential to the emergence of topological states.

V. EDGE STATES

To study the edge states in our mechanical dice lattice system, we assume hard walls along the zigzag edges to form a ribbon structure and impose the periodic boundary condition along the perpendicular direction. Of particular interest is whether the restriction will induce a gap at the degenerate points. We find that in most cases, a gap will indeed open due to the confinement. However, gapless states localized at the edge of the ribbon can arise [e.g., for the states at the bottom of Figs. 2(a) and 2(f)].

Figures 4(a) and 4(b) show ribbon band structures corresponding to the bulk band structures in Figs. 2(e) and 2(j), respectively. It can be seen that the density of states is finite along the bulk degenerate energy value, the behavior of which is typical of gapless edge states in topologically nontrivial materials [2–4,6,15,16]. These edge states have quite different behaviors from those of the nearby bulk states. To check

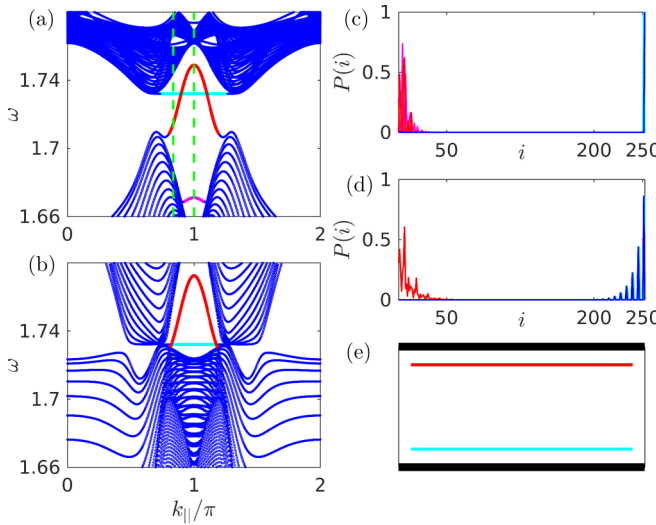


FIG. 4. Ribbon band structure and edge states in three- and two-band degenerate configurations. (a) Ribbon band structure corresponding to the three-band degenerate bulk configuration in Fig. 2(e). (b) Ribbon band structure corresponding to the two-band degenerate bulk configuration in Fig. 2(j). (c, d) Weight distributions of the edge states along index i of mass points in one unit cell. The corresponding bands are marked by the same color in (a, b). (e) A schematic illustration of the polarization of the edge states.

whether the bands are localized on the edge, we calculate the weight distribution of the wave function along the confinement direction of one unit cell, as shown in Figs. 4(c) and 4(d). In the simulation, there are 252 mass points within one unit cell which are marked consecutively from one end to the other. Figure 4(a) shows that there are three major bands with unique behaviors (marked by red, cyan, and magenta). Figure 4(b) shows the ribbon band structure with a two-band degeneracy [with the corresponding bulk band structure indicated as the bottom line in Fig. 2(j)]. We choose an arbitrary momentum value at which the bands appear and plot the real space distributions in Fig. 4(c), which indicate that these bands indeed are associated with edge states. To verify the level crossing phenomenon between the red and cyan bands, we choose a momentum value before and after the crossing points and find that the localization behavior does not change about the crossing points, i.e., the red and cyan band edge states are localized on different edges. A schematic illustration is presented in Fig. 4(e). A magnification of the flatband at about $\omega = \sqrt{3}$ in Fig. 4(a) reveals that there are in fact two degenerate flatbands: one marked by cyan and the other by blue. The states associated with the two degenerate bands are localized on the same edge, i.e., the opposite side of the red and magenta edge states. Such edge states arise for both $\eta_1 = 0$ and $\eta_1 = 0.5$ cases.

The gradient of the red edge states ensures the existence of at least one conducting channel about the bulk degenerate energy. As the conducting channels are located at the opposite side of the nonconducting channels for the edge states, in the physical space conduction occurs only along one side. From Fig. 1, we see that there is no inversion symmetry along the vertical direction in the general case where the two subsets of

springs are nonidentical, making this type of asymmetric edge states possible. We also find that a level crossing behavior can occur in a finite parameter region. For example, for $\eta_1 = 0$, an examination of the ribbon band structure reveals a level crossing behavior for $1.41 < \eta_2 < 1.67$. For larger values of η_2 , the red state becomes flat and coincides with the blue band, leading to two edge states with the same frequency but localized at different edges. For other highly degenerate phases, the confinement effect will open a gap in the ribbon band structure. However, edge states connecting the projections of the K and K' valleys persist.

VI. CONCLUSION

For ideal graphene or graphenelike 2D materials with a pair of Dirac cones connecting at a single point, the Berry curvature is zero. As a result, such materials in the metallic phase are incapable of generating nontrivial topological states. Is it possible to have 2D semimetals with a finite Berry curvature? Equivalently, is it possible for a 2D material to possess topological quantum phases without a gap opening even in the presence of symmetry breaking so that the quasiparticles remain massless? This paper provides an affirmative answer to this question.

We articulate a mechanical dice lattice system and analyze its band structure. In our system, there is a natural inversion symmetry breaking but the time-reversal symmetry is preserved. We find both three-band and two-band conical-like degeneracies and provide analytical insights into the emergence of the associated degenerate points in the absence of inversion symmetry. Due to the breaking of the inversion symmetry, the Berry curvature in the momentum space is generally finite, especially about the K and K' valleys, leading to a topologically nontrivial band structure and, consequently, to an anomalous valley Hall effect. As the degenerate points remain to be degenerate (i.e., no gap opening) even in the presence of an inversion symmetry breaking, the dice lattice system is effectively a *mechanical topological semimetal with massless quasiparticles*. We also study the confinement effect and find gapless edge states at the degenerate energy. In certain regions of the parameter space, between the projections of the K and K' valleys, conducting edge channels associated with a particular edge can arise while the opposite edge is nonconducting. A direct extension of our work to the case of rotating mechanical dice lattice would be worth pursuing, as the rotation will break the time-reversal symmetry so that a finite Chern number and topological protected edge states can arise.

ACKNOWLEDGMENTS

The authors would like to acknowledge support from the Vannevar Bush Faculty Fellowship program sponsored by the Basic Research Office of the Assistant Secretary of Defense for Research and Engineering and funded by the Office of Naval Research through Grant No. N00014-16-1-2828. This work was also supported by ONR under Grant No. N00014-15-1-2405.

APPENDIX

We present calculations of the band structure of our mechanical dice lattice. The starting point is Eqs. (2) and (3). Since our focus is on the band structure about the K and K' points, we set the momentum to that of the K point to obtain six energy levels, which depend on the parameters κ_2 , η_1 , and η_2 ($\kappa_1 = 1$). By setting $\eta_1 = 0$ and letting three of the six energy levels have the same energy, we can obtain an expression of the Berry curvature for the three-band degenerate phase. The formula for the two-band degenerate phase can be derived in a similar manner, with some specific value of η_1 . To proceed, we first expand the dynamic matrix Eq. (3) about the $K = [2\pi/(3a), 2\pi/(\sqrt{3}a)]$ point and introduce (dk_x, dk_y) through

$$k_x = \frac{2\pi}{3a} + dk_x, k_y = \frac{2\pi}{\sqrt{3}a} + dk_y.$$

Neglecting higher-order terms of (dk_x, dk_y) , we have that the off-diagonal parts of the dynamic matrix are changed to

$$\Gamma_{ab}(dk_x, dk_y) = \begin{pmatrix} \frac{3\eta_1}{4} - i\frac{\sqrt{3}(\eta_1-4)}{8}dk_y + \frac{\sqrt{3}(\eta_1-4)}{8}dk_x & i\frac{3\eta_1}{4} - \frac{3\sqrt{3}\eta_1}{8}dk_y + i\frac{\sqrt{3}\eta_1}{8}dk_x \\ i\frac{3\eta_1}{4} - \frac{3\sqrt{3}\eta_1}{8}dk_y + i\frac{\sqrt{3}\eta_1}{8}dk_x & -\frac{3\eta_1}{4} - i\frac{\sqrt{3}(3\eta_1-4)}{8}dk_y + \frac{\sqrt{3}(3\eta_1-4)}{8}dk_x, \end{pmatrix}$$

and

$$\begin{aligned} \Gamma_{bc}(dk_x, dk_y) \\ = \kappa_2 \begin{pmatrix} i\frac{3(i+\sqrt{3})\eta_2}{8} + \frac{(i\sqrt{3}+3)(\eta_2-1)}{4}dk_y + \frac{2(\sqrt{3}-3i)+(3i+\sqrt{3})\eta_2}{8}dk_x & -\frac{3(i+\sqrt{3})\eta_2}{8} + i\frac{(3i+\sqrt{3})\eta_2}{8}dk_x \\ -\frac{3(i+\sqrt{3})\eta_2}{8} + i\frac{(3i+\sqrt{3})\eta_2}{8}dk_x & -i\frac{3(i+\sqrt{3})\eta_2}{8} - i\frac{(-3i+\sqrt{3})}{4}dk_y + \frac{-2(3i-\sqrt{3})+(3i-3\sqrt{3})\eta_2}{8}dk_x \end{pmatrix}. \end{aligned}$$

From the expressions of Γ_{ab} and Γ_{bc} , we see that each matrix element contains an $O(1)$ term, which is proportional to the values of η_1 and η_2 , as well as $O(dk)$ terms. Physically, Γ_{ab} and Γ_{bc} quantify the coupling between the nonequivalent mass points. As a result, in the limit $\eta_1 = 0$, the coupling between the mass points a and b is at most a first-order quantity. (In fact, the value η controls the interplay between the longitudinal and transverse wave modes [23].) Note that, in a mechanical graphene system, in the limit $\eta = 0$ there is no distinction between the longitudinal and transverse waves so that the system possesses a twofold degenerate dispersion relation typical of the nearest-neighbor tight-binding graphene system. However, in our mechanical dice lattice, even for $\eta_1 = 0$, there is still coupling between the mass points (the blue and red points in Fig. 1) through the finite values of κ_2 and η_2 . As a result, we expect richer physical phenomena to arise in the dice lattice system than in the mechanical graphene system. In fact, insofar as $\eta_2 \neq 0$, Γ_{bc} will contribute an $O(1)$ order coupling between the blue (b) and red (c) mass points. Note that, setting $\kappa_2 = 0$ reduces the mechanical dice lattice to a mechanical graphene system.

To calculate the Berry curvature about the K point, we need the Bloch wave functions, which is difficult to be calculated analytically for 6×6 matrices. However, for $\eta_1 = 0$, the influence of the mass point a on the mass points b, c can be neglected, as $\Gamma_{ab} \approx O(dk)$. We thus obtain a 4×4 reduced matrix:

$$\tilde{\Gamma}(dk) = \begin{bmatrix} \Lambda_1 + \Lambda_2 & \Gamma_{bc}(dk) \\ \Gamma_{bc}^\dagger(dk) & \Lambda_2 \end{bmatrix}.$$

For this reduced dynamic matrix, analytical expressions for the eigenfunctions can be obtained from which the Berry curvature can be calculated. Figure 3(g) shows the Berry curvature along $k_y = 2\pi/(\sqrt{3}a)$, where the parameters are $\kappa_2 = 3/2$ and $\eta_2 = 1/2$. The analytic expression for the Berry curvature is

$$\Omega(dk_x) = \tau_z(1.2 - 7.43dk_x^2),$$

where $\tau_z = 1(-1)$ for the $K(K')$ point. Note that these analytic expressions of the Berry curvature hold only for momentum values not in the immediate vicinities of the Dirac points.

-
- [1] K. von Klitzing, *Rev. Mod. Phys.* **58**, 519 (1986).
 - [2] M. Z. Hasan and C. L. Kane, *Rev. Mod. Phys.* **82**, 3045 (2010).
 - [3] X.-L. Qi and S.-C. Zhang, *Rev. Mod. Phys.* **83**, 1057 (2011).
 - [4] C. L. Kane and E. J. Mele, *Phys. Rev. Lett.* **95**, 226801 (2005).
 - [5] A. Bansil, H. Lin, and T. Das, *Rev. Mod. Phys.* **88**, 021004 (2016).
 - [6] Y. Ren, Z. Qiao, and Q. Niu, *Rep. Prog. Phys.* **79**, 066501 (2016).
 - [7] D. Xiao, M.-C. Chang, and Q. Niu, *Rev. Mod. Phys.* **82**, 1959 (2010).
 - [8] M.-C. Chang and Q. Niu, *Phys. Rev. B* **53**, 7010 (1996).
 - [9] G. Sundaram and Q. Niu, *Phys. Rev. B* **59**, 14915 (1999).
 - [10] D. Xiao, W. Yao, and Q. Niu, *Phys. Rev. Lett.* **99**, 236809 (2007).
 - [11] N. Nagaosa, J. Sinova, S. Onoda, A. H. MacDonald, and N. P. Ong, *Rev. Mod. Phys.* **82**, 1539 (2010).
 - [12] K. S. Novoselov, A. K. Geim, S. V. Morozov, D. Jiang, Y. Zhang, S. V. Dubonos, I. V. Grigorieva, and A. A. Firsov, *Science* **306**, 666 (2004).
 - [13] K. Novoselov, A. K. Geim, S. Morozov, D. Jiang, M. Katsnelson, I. Grigorieva, S. Dubonos, and A. Firsov, *Nature (London)* **438**, 197 (2005).
 - [14] F. D. M. Haldane, *Phys. Rev. Lett.* **61**, 2015 (1988).

- [15] F. Zhang, J. Jung, G. A. Fiete, Q. Niu, and A. H. MacDonald, *Phys. Rev. Lett.* **106**, 156801 (2011).
- [16] F. Zhang, A. H. MacDonald, and E. J. Mele, *Proc. Natl. Acad. Sci. USA* **110**, 10546 (2013).
- [17] G. Palumbo and K. Meichanetzidis, *Phys. Rev. B* **92**, 235106 (2015).
- [18] X. Wan, A. M. Turner, A. Vishwanath, and S. Y. Savrasov, *Phys. Rev. B* **83**, 205101 (2011).
- [19] S.-Y. Xu, I. Belopolski, N. Alidoust, M. Neupane, G. Bian, C. Zhang, R. Sankar, G. Chang, Z. Yuan, C.-C. Lee, S.-M. Huang, H. Zheng, J. Ma, D. S. Sanchez, B. Wang, A. Bansil, F. Chou, P. P. Shibayev, H. Lin, S. Jia, and M. Z. Hasan, *Science* **349**, 613 (2015).
- [20] B. Q. Lv, H. M. Weng, B. B. Fu, X. P. Wang, H. Miao, J. Ma, P. Richard, X. C. Huang, L. X. Zhao, G. F. Chen, Z. Fang, X. Dai, T. Qian, and H. Ding, *Phys. Rev. X* **5**, 031013 (2015).
- [21] S. M. Young, S. Zaheer, J. C. Y. Teo, C. L. Kane, E. J. Mele, and A. M. Rappe, *Phys. Rev. Lett.* **108**, 140405 (2012).
- [22] C.-Z. Xu, Y.-H. Chan, Y. Chen, P. Chen, X. Wang, C. Dejoie, M.-H. Wong, J. A. Hlevyack, H. Ryu, H.-Y. Kee, N. Tamura, M.-Y. Chou, Z. Hussain, S.-K. Mo, and T.-C. Chiang, *Phys. Rev. Lett.* **118**, 146402 (2017).
- [23] T. Kariyado and Y. Hatsugai, *Sci. Rep.* **5**, 18107 (2015).
- [24] Y.-T. Wang, P.-G. Luan, and S. Zhang, *New J. Phys.* **17**, 073031 (2015).
- [25] Y. Liu, Y. Xu, S.-C. Zhang, and W. Duan, [arXiv:1606.08013](https://arxiv.org/abs/1606.08013).
- [26] Z.-G. Chen and Y. Wu, *Phys. Rev. Appl.* **5**, 054021 (2016).
- [27] H. C. Po, Y. Bahri, and A. Vishwanath, *Phys. Rev. B* **93**, 205158 (2016).
- [28] E. Prodan and C. Prodan, *Phys. Rev. Lett.* **103**, 248101 (2009).
- [29] L. Zhang, J. Ren, J.-S. Wang, and B. Li, *Phys. Rev. Lett.* **105**, 225901 (2010).
- [30] C. L. Kane and T. C. Lubensky, *Nat. Phys.* **10**, 39 (2014).
- [31] L. M. Nash, D. Kleckner, A. Read, V. Vitelli, A. M. Turner, and W. T. M. Irvine, *Proc. Natl. Acad. Sci. USA* **112**, 14495 (2015).
- [32] P. Wang, L. Lu, and K. Bertoldi, *Phys. Rev. Lett.* **115**, 104302 (2015).
- [33] R. Süsstrunk and S. D. Huber, *Science* **349**, 47 (2015).
- [34] D. Z. Rocklin, B. Gin-ge Chen, M. Falk, V. Vitelli, and T. C. Lubensky, *Phys. Rev. Lett.* **116**, 135503 (2016).
- [35] E. Prodan, K. Dobiszewski, A. Kanwal, J. Palmieri, and C. Prodan, *Nat. Commun.* **8**, 14587 (2017).
- [36] S. D. Huber, *Nat. Phys.* **12**, 621 (2016).
- [37] A. Raoux, M. Morigi, J.-N. Fuchs, F. Piéchon, and G. Montambaux, *Phys. Rev. Lett.* **112**, 026402 (2014).
- [38] B. Bradlyn, J. Cano, Z. Wang, M. G. Vergniory, C. Felser, R. J. Cava, and B. A. Bernevig, *Science* **353**, aaf5037 (2016).
- [39] Z. Zhu, G. W. Winkler, Q. S. Wu, J. Li, and A. A. Soluyanov, *Phys. Rev. X* **6**, 031003 (2016).
- [40] L. Zhang and Q. Niu, *Phys. Rev. Lett.* **115**, 115502 (2015).
- [41] Y.-T. Wang and S. Zhang, *New J. Phys.* **18**, 113014 (2016).